Available online at www.sciencedirect.com
ScienceDirect
International Journal of Multiphase Flow 33 (2007) 300–316
International Journal of Multiphase Flow
www.elsevier.com/locate/ijmulflow

On the liquid turbulence energy spectra in two-phase bubbly flow in a large diameter vertical pipe

M.E. Shawkat, C.Y. Ching *, M. Shoukri

Department of Mechanical Engineering, McMaster University, 1280 Main Street West, Hamilton, Ont., Canada L8S4L7

Received 15 February 2006; received in revised form 1 September 2006

Abstract

The liquid turbulence structure of air–water bubbly flow in a 200 mm diameter vertical pipe was experimentally investigated. A dual optical probe was used to measure the bubble characteristics, while the liquid turbulence was measured using hot-film anemometry. Experiments were performed at two liquid superficial velocities of 0.2 and 0.68 m/s for gas superficial velocities in the range of 0–0.18 m/s, corresponding to an area averaged void fraction up to 13.6%. In general, there is an increase in the liquid turbulence energy when the bubbles are introduced into the liquid flow. The increase in the energy mainly occurs over a range of length scales that are on the order of the bubble diameter. A suppression of the turbulence was observed close to the wall at very low void fraction flows. Initially, the suppression occurs in the low wave number range and then extends to higher wave numbers as the suppression is increased.

Keywords: Two-phase flow; Turbulence; Energy spectra; Length scale

1. Introduction

In two-phase bubbly flows, the interaction between the gas bubbles and the liquid turbulence plays a major role in mass, momentum, and energy transfer between the phases. There is a two-way interaction between the bubbles and the liquid turbulence, where the gas bubbles can either augment or suppress the liquid turbulence (Serizawa and Kataoka, 1990). It has been observed that in large diameter vertical pipes (diameter typically greater than 150 mm), the bubbles tend to migrate toward the centerline forming "core-peak" distributions for the void fraction, bubble frequency and interfacial area concentration, instead of the "wall-peak" distributions usually found in smaller diameter pipes for the corresponding flow conditions (e.g., Ohnuki and Akimoto, 2000; Yoneda et al., 2002; Shoukri et al., 2003; Sun et al., 2003). Lahey Jr. et al. (1993) suggested that one factor which determines the direction of bubble migration is the diffusion effect of the liquid turbulence on the bubbles. He introduced this effect in the form of a force called "turbulent dispersion force", defined as

* Corresponding author. Tel.: +1 905 545 9140x24998; fax: +1 905 572 7944.
E-mail address: chingcy@mcmaster.ca (C.Y. Ching).

0301-9322/$ - see front matter © 2006 Elsevier Ltd. All rights reserved.
doi:10.1016/j.ijmultiphaseflow.2006.09.002

the summation of all fluctuating force components on the bubble motion (Lopez de Bertodano, 1998). Ohnuki and Akimoto (2000) suggested that in upward bubbly flow this force has the potential to counter the effect of the lift force and move the bubbles towards the centerline.

For a better understanding of the bubble–liquid turbulence interaction, it is important to study the structure of the liquid turbulence under both wall and core-peak distributions. Most previous investigations on the liquid turbulence structure in bubbly flows have been performed in small diameter pipes, where the relations between the turbulence length scales, energy spectra, and the bubble characteristics have been presented. Michiyoshi and Serizawa (1986), Gore and Crowe (1989), Wang et al. (1990) and Lance and Bataille (1991) presented the effect of different flow parameters on the turbulence length scales and the energy spectra for bubbly flows. No systematic relation was observed by Michiyoshi and Serizawa (1986) to describe the radial distributions of the integral and dissipation length scales. In general, increasing the void fraction was found to decrease the area averaged integral length scale due to the break-up of the continuous liquid phase by the gas bubbles. For example, Wang et al. (1990) showed that the area under the auto-correlation curves at the pipe centerline, which is related to the integral length scale, decreased as the void fraction increased. Liu (1989) found the integral length scale was approximately constant in the core region and decreased near the wall. The same trend was confirmed by Ohnuki and Akimoto (2001) in a large diameter pipe for an almost uniform void fraction profile. However, currently there is no extensive experimental data or general relations to estimate the integral length scale as a function of the flow parameters as in single-phase flow. Wang et al. (1990) showed that the dissipation and Kolomogrov length scales at the pipe centerline also decreased with an increase of void fraction, and their values were smaller than the corresponding single-phase values. Liu (1989) showed that this was true at all radial locations and not only at the pipe centerline.

There is a change in the liquid turbulence energy spectrum in bubbly flows due to the interaction of the bubbles with the turbulence. This interaction is expected to be most prevalent in the range of turbulence length scales that are comparable to the bubble diameter. Michiyoshi and Serizawa (1986), Wang et al. (1990) and Lance and Bataille (1991) found that the slope of the liquid turbulence energy spectra was $(-8/3)$ in the inertial region, which is higher than the traditional value of $(-5/3)$ for single-phase flow. Michiyoshi and Serizawa (1986) derived the $(-8/3)$ slope from a simple dimensional analysis for the spectra, with the bubble diameter (D_b) as an extra length scale. Wang et al. (1990) noticed a discontinuity in the energy spectra, and suggested that two length and velocity scales should be used to model the liquid turbulence conservation equations. Michiyoshi and Serizawa (1986) measured the radial fluctuating velocity, and found that the spectra had the same trend as the axial spectra, but with a lower amplitude. Rensen et al. (2005) suggested that the main parameter that governs the slope of the spectra was the bubblance, defined as the ratio between the energy added to the liquid flow by the bubbles and the initial single-phase turbulence energy ($0.5\alpha U_r^2/u_{sp}^2$), where α is the void fraction, U_r the relative velocity, and u_{sp} is the turbulent velocity of the single-phase flow. By examining experimental data, they concluded that a slope of $(-8/3)$ was associated with bubblance greater than one. The database they used was based on experiments in small diameter pipes and in large conduits but with small void fraction values that ranged up to 2.5%.

The objective of this paper is to experimentally investigate the bubble–liquid turbulence interaction of bubbly flow in a large diameter pipe. In particular, the energy spectra for the axial and radial turbulent fluctuations were used to examine the turbulence energy cascade in such flows. The experiments were performed in a 200 mm diameter vertical pipe for upward air–water flow at two liquid superficial velocities (J_f) of 0.2 and 0.68 m/s, and gas (J_g) superficial velocities in the range 0.005–0.18 m/s. The area averaged void fraction ($\langle\alpha\rangle$) corresponding to these flow conditions was between 1.2% and 13.6%.

2. Test facilities

The experiments were performed in a 200 mm diameter closed two-phase flow loop shown schematically in Fig. 1. The main vertical test section or the riser is 9.56 m in length. The air is introduced through a showerhead injector that has 550 holes of 1 mm diameter spread evenly over the area of the riser inlet. A honeycomb flow straightener and a coarse grid mesh were installed downstream of the injector to reduce the bubble swirl and improve bubble distribution. Air is completely removed in the separation tank at the end of the riser and single phase water flows back to the pump through the downcomer pipe. A heat exchanger connected to a

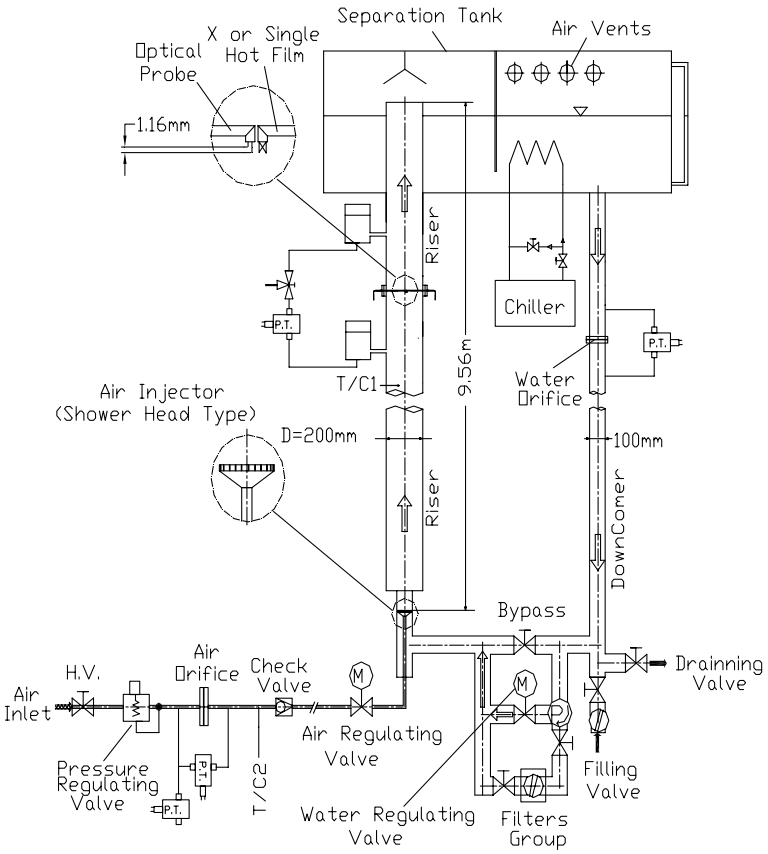

Fig. 1. Schematic of experimental test facility.

dedicated chiller is installed in the main phase separation tank to maintain the water temperature steady at 24.5 ± 0.1 °C within the flow loop during the experiments. Water and air flow rates are measured using sharp edge orifices installed in the downcomer and the inlet air line respectively. Two pneumatic valves on the water and air lines are used to control the flow rates remotely. The axial pressure gradient was measured along the pipe axis under different flow conditions. Its value was found to be nearly constant beyond 32 pipe diameters from the point of air injection, indicating that the flow is fully developed beyond this location.

A dual optical probe was used to measure the bubble characteristics at different radial locations. The horizontal and vertical distances between the probe tips were 1 and 1.16 mm respectively. A single TSI 1210-60W hot film and a Dantec 55R63 X-hot film were used to measure the turbulence characteristics. The overheat ratios for the single and cross hot films were 1.08 and 1.06, respectively. Both the optical and the hot film probes were mounted on individual traverse mechanisms with a resolution of 0.01 mm. Measurements with the optical and single hot film were made along the radial direction up to a relative radius (r/R) of 0.99, while the cross hot-film was traversed up to r/R of 0.95 due to its spatial limitations. All measurements were performed at a vertical distance of 42 diameters downstream from the point of air injection. Data were acquired at a sampling frequency of 10 kHz using a 16 bit A/D converter interfaced to a PC using Lab View software. The signals were sampled for 80 s, which was found sufficient to obtain statistically steady values. At very low air flow rates, however, a sampling time of 120 s was used due to the smaller bubble population in this case.

The hot films were calibrated in the flow loop operated with only single-phase water. The probes were placed at the centerline and the velocity was obtained from the flow rate assuming a $(1/n)$ power law distribution for the velocity profile, where $n = 2.95Re^{0.0805}$ (Schlichting, 1979). For the cross hot-film, the yaw calibrations were performed using the effective angle concept of Browne et al. (1989). A special fixture was designed and fabricated for the cross hot-film probe to perform the yaw-calibration, which allowed the probe

to yaw ±33° while ensuring the probe was at the pipe centerline for all yaw angles. The accuracy of the yaw calibration was checked by comparing the cross and the single hot film measurements in single and two-phase flows. In both flows the discrepancy in the average liquid velocity was less than ±3%. The discrepancy in the axial turbulent velocity for single-phase flow was about ±2.5%, while for the two-phase flow it increased to about ±8%, especially in high void fraction flows. This relatively larger discrepancy in two-phase flow is likely due to errors in the phase separation technique, where the detection of the trailing interfaces of the bubbles in the cross hot-film signal is more difficult due to the inclination of the film, which results in a less sharp change in the signal at the bubble trailing interfaces.

The reliability of the single and cross hot-film measurements were checked by performing a number of single-phase measurements using only water and comparing the average liquid and turbulent velocities, (U) and (u' and v'), with the experimental data of Laufer (1954), Lawn (1971) and Browne and Dinkelacker (1995). The average velocity and turbulent intensities were in good agreement with the experimental data, with a maximum deviation near the wall ($r/R > 0.95$) of approximately ±6% for the average velocity and ±10% for the turbulent intensities.

3. Signal processing and data reduction

The operation of the optical probe is based on the difference of the light refractive index between the liquid and gas phases. The reflected light at the probe tip is converted to a voltage through a photo-multiplier, which varies between a maximum value, corresponding to the gas phase, and a minimum value corresponding to the liquid phase. A combined amplitude and slope threshold method was adopted to separate the signal into the two phases. A train of unit pulses was used to replace the gas phase signal, where the pulse width represents the contact time between the probe tip and the gas phase. The local void fraction was obtained as the ratio between the summation of the time occupied by the pulses and the total sampling time. The void fraction presented in this study were obtained from the front optical probe, and these results were within ±3% of those determined from the rear probe. The local void fraction obtained by the optical probe was within ±10% of that obtained using the hot-film sensor at the same radial location.

The bubble velocity (U_b) was estimated from the time taken for the bubble front to travel between the two probe tips. The signals were filtered using the method of Revankar and Ishii (1992) to ensure that only bubbles that hit both probe tips were used to estimate the velocity. The bubble chord length of each bubble passing the probes was then estimated as

$$x_b = \Delta t \cdot U_b \tag{1}$$

where Δt is the time occupied by the width of each unit pulse. The nominal bubble diameter was estimated as the average of the chord lengths that represent the bubble diameter by further filtering the signals to exclude bubbles that hit the probe away from the bubble center. The bubble diameter was also calculated using the normalized chord length probability density function (PDF(x_b)) of the unfiltered signals, as suggested by Uga (1972) and Liu (2002),

$$D_b = 1.5 \int_0^\infty x_b \cdot \mathrm{PDF}(x_b)\, \mathrm{d}x_b \tag{2}$$

The results from the two methods agreed to within ±4.5%.

In the hot film signal, there is a sharp drop in the voltage signal as a bubble passes through the hot film sensor because the heat transfer coefficient in the gas phase is significantly less than that in the liquid phase. Details of the change in the voltage signal as a bubble penetrates the hot film sensor is described by Bruun (1995). To obtain the liquid turbulence characteristics, the signal corresponding to the liquid and gas phases should be identified and separated. Two main techniques have been developed to perform this operation; a combined amplitude and slope threshold method (Liu and Bankoff, 1993; Farrar et al., 1995; Wang and Ching, 2001), and more recently a pattern recognition method (Rensen et al., 2005). The voltage signal corresponding to the gas phase in the current experiments was identified and removed using the combined amplitude and slope threshold method as described by Wang and Ching (2001) and Farrar et al. (1995). In this

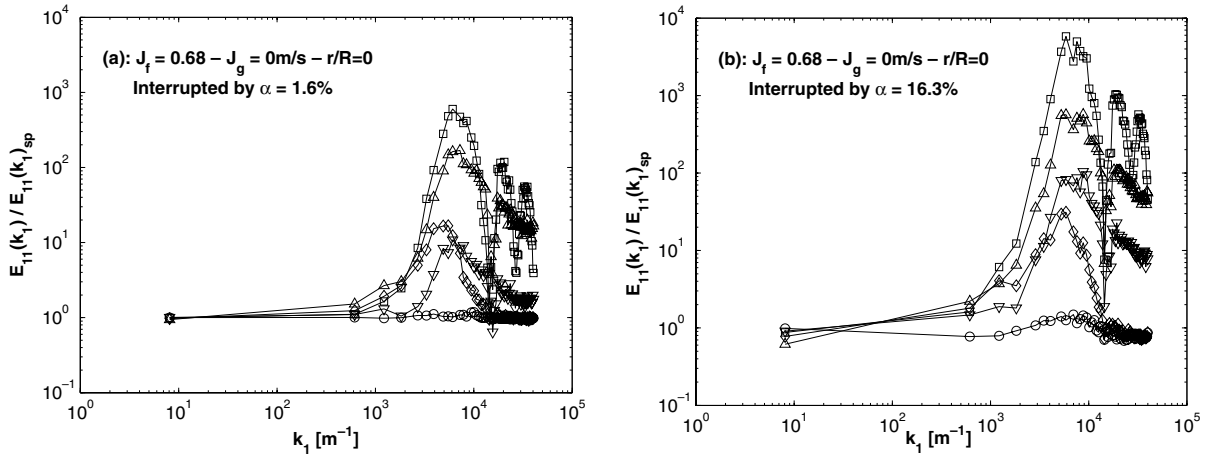

Fig. 2. Effect of replacing the gaps in the hot film signal on the energy spectra for α (a) 1.6% and (b) 16.3% ((∇) direct connection, (□) with a moving average at the connecting points, (△) with the mean and without a hanning window, (◇) with the mean and a hanning window, (○) linear interpolation).

method, an appropriate amplitude threshold is first used to detect the voltage drop due to the passage of a bubble and then a slope threshold is used to specify the front and the back of the bubble.

Five different methods were investigated to replace the subsequent gaps in the signal such that the liquid turbulence statistics and spectra were not affected. These are: (1) removing the gaps and directly connecting the portions of the signal corresponding to the liquid phase, (2) using a moving average to smooth the signal at the connection points, (3) replacing the gaps with the mean value of the liquid signal, (4) using a hanning window with the previous method, and (5) replacing the gaps with a linear interpolation using the same number of removed points. The effect of these methods on the average and turbulent liquid velocities, and turbulence spectra was examined at different flow conditions by interrupting, electronically, single-phase signals using a gas identifier signal (X) of a two-phase signal, where X is one for the liquid phase and zero for the gas phase. Two gas identifier signals corresponding to a low and high local void fraction flow of 1.6% and 16.3% were used, which corresponds to the current range of experimental conditions. All the methods did not have a significant effect on the mean value. At high void fraction, using the moving average technique overestimated the turbulent velocity by approximately 2.5%, while replacing the gaps with the mean underestimated it by approximately 12%. When a hanning window was applied, the uncertainty decreased to approximately 7.8%. Methods 1 and 5 did not have a significant effect on the root mean square value. The ratio of the energy spectra between the interrupted signal ($E_{11}(k_1)$) and the original single-phase signal ($E_{11}(k_1)_{sp}$) using the different techniques are shown in Fig. 2. It is clear that the linear interpolation technique (method 5) has the minimum deviation from the original spectra, especially at the high wave number range. All other methods result in a bias in the spectra at the high wave number range. Hence, in the current study, a linear interpolation was used to obtain a continuous liquid hot film signal to estimate the different turbulence characteristics.

4. Results and discussion

4.1. Void fraction and bubble diameter

The radial void fraction distributions at liquid superficial velocities of 0.2 and 0.68 m/s for different gas superficial velocities are shown in Fig. 3. For J_f of 0.2 m/s and at the lowest J_g of 0.005 m/s (Fig. 3(a)), the void fraction profile is nearly uniform and displays a slight increase near the pipe wall. As J_g is increased, the bubbles tend to migrate toward the pipe centerline and the profiles show more of a core-peak distribution. At the higher value of J_f and lowest J_g the profile has a more pronounced wall-peak, as shown in Fig. 3(b).

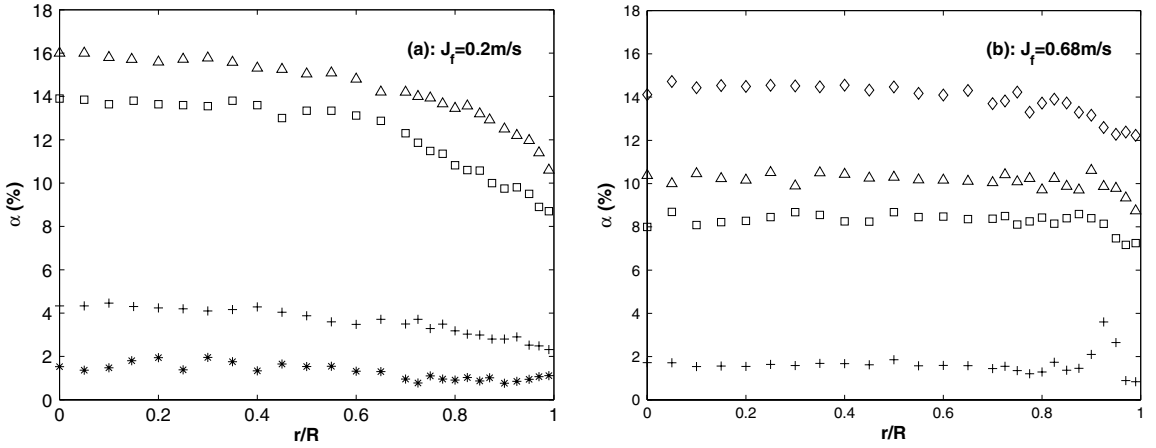

Fig. 3. Radial distribution of the void fraction at J_f (a) 0.2 and (b) 0.68 m/s for J_g of (∗) 0.005, (+) 0.015, (□) 0.085, (△) 0.1, and (◊) 0.18 m/s.

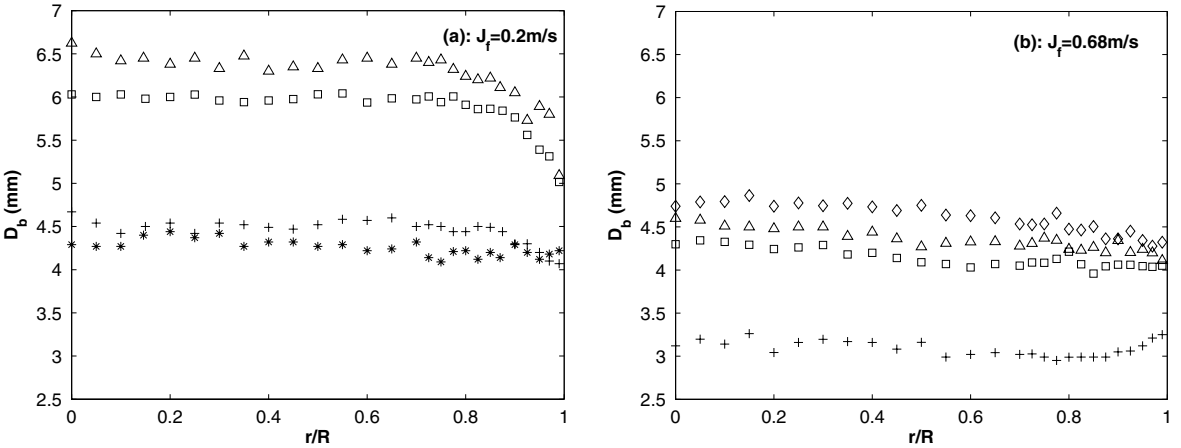

Fig. 4. Radial distribution of the bubble diameter at J_f (a) 0.2 and (b) 0.68 m/s for J_g of (∗) 0.005, (+) 0.015, (□) 0.085, (△) 0.1, and (◊) 0.18 m/s.

Increasing J_g in this case results in the profiles becoming more uniform, and tending towards a core peak distribution. The area average void fraction for which a wall peak profile was observed is about 1.4%.

The corresponding bubble diameter distributions are shown in Fig. 4. For both J_f, an increase in the gas flow rate results in larger bubble sizes. The bubble diameter profiles, to a large extent, show the same trends as the void distribution. For example, at $J_f = 0.2$ m/s and $J_g = 0.1$ m/s, the bubble diameter profile is relatively uniform through the pipe core region up to a relative radius of 0.8, and then decrease as the wall is approached, similar to the void fraction profile. When a distinct wall peak distribution is observed for the void fraction ($J_f = 0.68$ m/s, $J_g = 0.015$ m/s), the bubble diameter profile shows an increase toward the pipe wall. The increase in the diameter starts approximately at the location where the peak in the void is observed, and is likely due to bubble coalescence in this region.

4.2. Liquid average velocity, turbulence intensities and length scales

The radial distribution of the liquid average velocity normalized by the centerline value (U_{CL}) for the different flow conditions is presented in Fig. 5. The single phase data at the corresponding J_f are also shown for

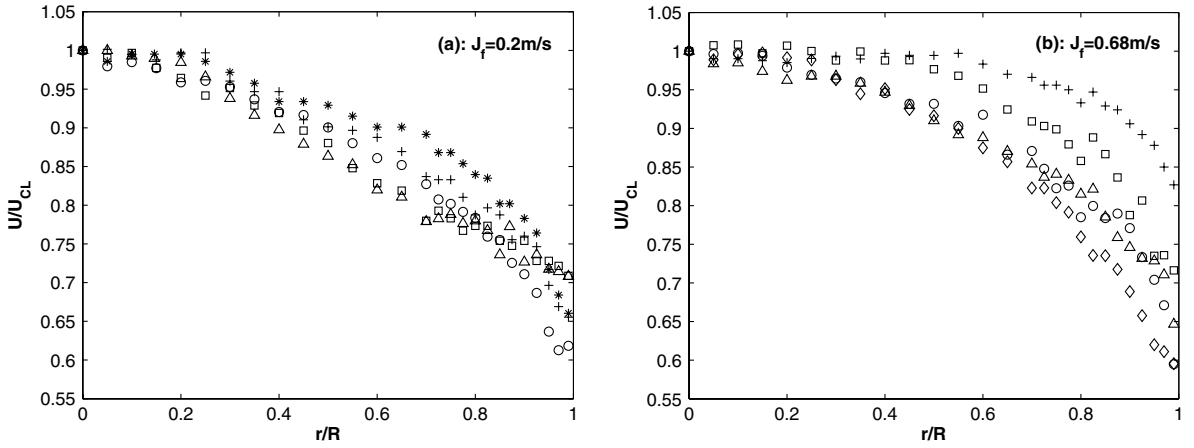

Fig. 5. Radial distribution of the liquid average normalized velocity at J_f (a) 0.2 and (b) 0.68 m/s for J_g of (○) 0.0, (*) 0.005, (+) 0.015, (□) 0.085, (△) 0.1, and (◇) 0.18 m/s.

comparison. For the lower J_f and at the lowest J_g, the void fraction profile is approximately uniform through the test section and the liquid velocity profile is very close to the single phase profile (Fig. 5(a)). As J_g increases and the void fraction profiles tend to a core peak, the average velocity in the central region becomes higher than that towards the wall, relative to the single phase case. However, at the higher J_f and lowest J_g of 0.015 m/s (Fig. 5(b)), where the void fraction shows a wall-peak, the (U/U_{CL}) profile is more uniform throughout the core of the pipe compared to the single phase data, and falls off much more rapidly as the wall is reached. Similar profiles were observed in small diameter pipes with wall peak void fraction profiles (e.g., Michiyoshi and Serizawa, 1986; Wang et al., 1987; Liu and Bankoff, 1993). In this case, it seems that the higher void towards the wall tends to increase the average liquid velocity in this region. As J_g increases and the void fraction profile becomes more uniform, the deviation of the velocity profile from the single phase flow becomes less. The data clearly shows that a higher local void fraction tends to increase the local average liquid velocity. This is due to the higher bubble velocity relative to the local liquid velocity, which will increase the local liquid velocity in the vicinity of the bubbles. The radial distribution of the relative velocity between the bubble and average liquid velocities ($U_r = U_b - U$) is shown in Fig. 6. For the lower J_f an increase in the gas flow rate increases the relative velocity throughout the pipe. However, for the higher J_f an increase in J_g, in general, decreases the relative velocity in the core of the pipe while increasing it near the pipe wall.

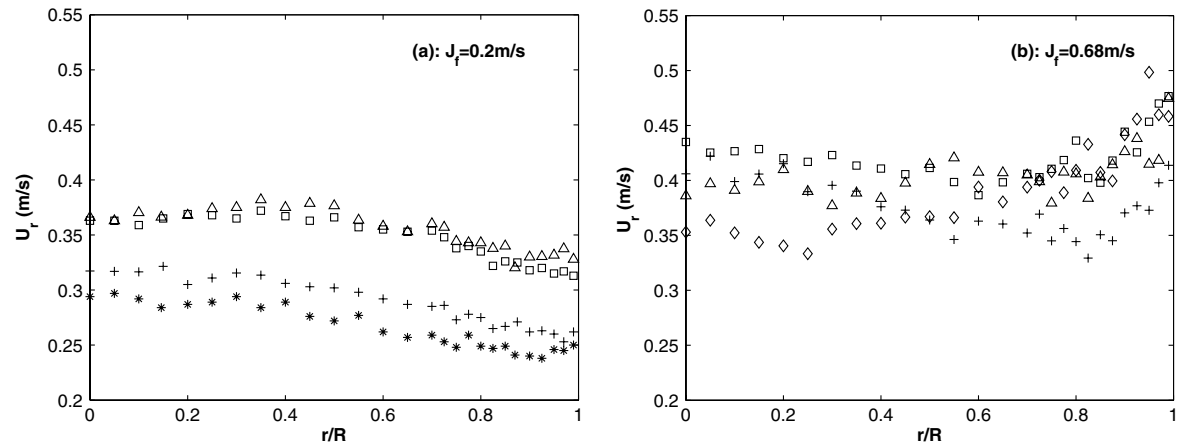

Fig. 6. Radial distribution of the relative velocity at J_f (a) 0.2 and (b) 0.68 m/s for J_g of (○) 0.0, (*) 0.005, (+) 0.015, (□) 0.085, (△) 0.1, and (◇) 0.18 m/s.

The liquid axial and radial turbulence intensity profiles (u'/U and v'/U) for the two J_f are shown in Fig. 7. The single-phase turbulence data corresponding to the same liquid superficial velocity J_f is shown for comparison. In general, increasing the gas flow rate increases the axial and radial turbulence intensity for all flow conditions. However, at $J_f = 0.68$ m/s and the lowest J_g of 0.015 m/s, a turbulence suppression relative to the single-phase flow is observed near the wall as shown in Fig. 7(b) and (d). For the lower J_f, as the bubbles are introduced at very low J_g, both the axial and radial turbulence intensities initially increase in the central core of the pipe, resulting in a profile that decreases toward the wall. As J_g is further increased, the turbulence intensity in the wall region increases relative to the core region, causing the profiles to be more uniform as shown in Fig. 7(a) and (c). For the higher J_f, the increase in the turbulence intensity near the wall relative to the core with increasing J_g is more pronounced and the shape of the profiles approaches that of the single-phase flow, as seen in Fig. 7(b) and (d). The development of the profiles with increasing J_g may be explained using the following argument. Kataoka and Serizawa (1989) suggested that the liquid turbulence production in two-phase flow is governed by two terms; namely the production due to the shear stress $\left(\rho_L(1-\alpha)\overline{u'v'}\frac{\partial U}{\partial r}\right)$ and a bubble-production term due to the relative velocity between the bubbles and the liquid. They modeled the bubble-production term as $(\rho_L C_D U_r^3 a_i)$, where C_D and a_i are the drag coefficient and the interfacial area concentration, respectively. The bubble-production term is then directly proportional to a_i, which has similar characteristics to the void fraction (e.g., Hibiki and Ishii, 1999; Shoukri et al., 2003) and to the cube power of the relative velocity. At the lower J_f, the void fraction and the relative velocity are higher in the core region, except at very low J_g, where the void fraction is nearly uniform. Hence, a higher

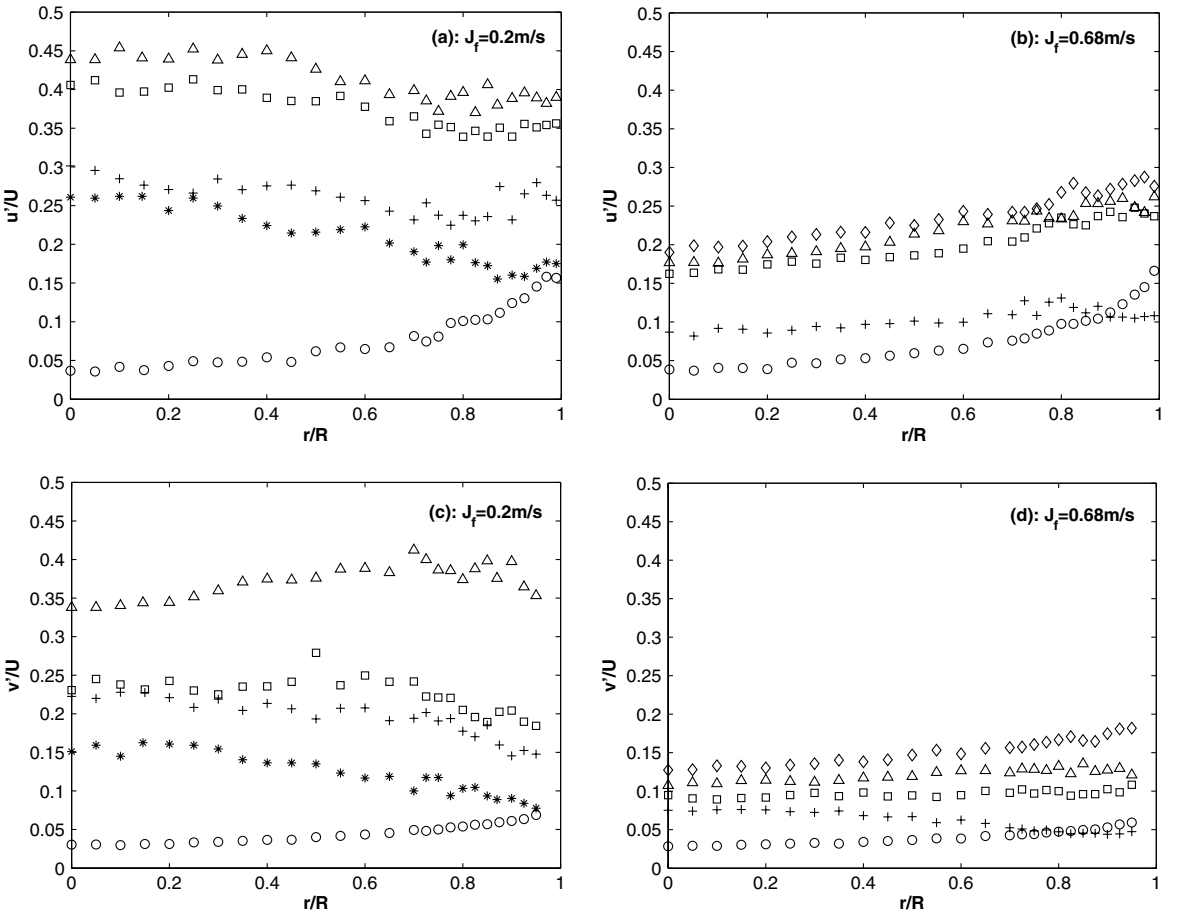

Fig. 7. Radial distribution of the liquid axial and radial turbulent intensities at J_f (a, c) 0.2 and (b, d) 0.68 m/s for J_g of (○) 0.0, (∗) 0.005, (+) 0.015, (□) 0.085, (△) 0.1, and (◇) 0.18 m/s.

turbulence energy production due to the bubbles can be expected in the core region compared to that near the wall, resulting in turbulent intensity profiles that are higher in the core region. At the higher J_f, however, the void fraction is more uniform, while the relative velocity shows an increase towards the wall. Hence, the turbulence production due to the bubbles will be more uniform or higher towards the wall in this case.

The longitudinal integral length scale (L_{11}) was calculated from the autocorrelation of the axial turbulent velocity ($R_{11}(\tau)$) using Taylor's frozen hypothesis as

$$L_{11} = U \int_0^\infty R_{11}(\tau)\,\mathrm{d}\tau \tag{3}$$

The autocorrelation functions at different flow conditions for single and two-phase flows at the pipe centerline are shown in Fig. 8. At a given J_f, an increase in J_g results in a decrease in the degree of the correlation indicating a smaller integral length scale. Moreover, since the curvature of the autocorrelation curve at $\tau = 0$ represents the dissipation length scale, an increase in J_g indicates a decrease in the dissipation length scale too. In the two-phase flow, negative values for the correlation coefficients were observed beyond a time lags of about 0.75 s, which was also reported by Liu (1989) in a smaller diameter pipe. The integration of Eq. (3) was performed numerically up to the time lag corresponding to $R_{11}(\tau) = 3.3\%$, as shown in Fig. 8. This criteria was found suitable for both single and two-phase flows at the different radial locations. The accuracy of this criteria was checked against the single-phase flows using the method of Van Fossen et al. (1995), where the autocorrelation curves were fit with an exponential curve $e^{-c\tau}$ for R_{11} between 1 and 0.33 to eliminate the effect of the small frequency noise. The agreement between the two methods was within ±10%. The values of L_{11} could be considered an approximation here, since the validity of Taylor's hypothesis in two-phase flow has not been verified.

The radial distributions of L_{11} normalized by the pipe radius R_{pipe} at the different flow conditions are shown in Fig. 9. For the single-phase flow, the normalized L_{11} decreases as the wall is approached, with a nearly constant value of about 0.2 in the central core of the pipe, and are consistent with previous measurements. As the liquid flow rate increased from J_f of 0.2–0.68 m/s (corresponding to Re from 46,700 to 158,700) the integral length scale increased by about 15%, especially near the wall. As the bubbles are introduced into the liquid flow, the integral length scale decreases relative to the single-phase value. This is expected due to the break-up of the continuous liquid phase by the gas bubbles. For example, the normalized integral length scale at the centerline decreases from about 0.2 to about 0.12 at the highest void fraction. The change in length scales could also be attributed to the wakes of the bubbles that arise from the relative velocity between the bubbles and the liquid.

At the lower J_f, the length scale decreases in the radial direction towards the wall (Fig. 9(a)); however, at the higher J_f the integral length scale tends to increase up to about $r/R \approx 0.8$, and then decreases toward the pipe

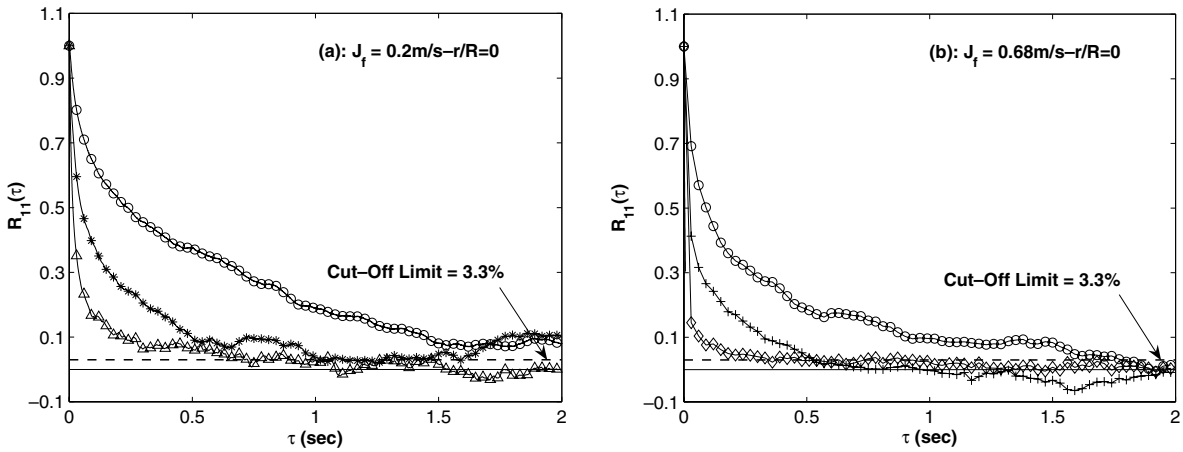

Fig. 8. The autocorrelation function at the pipe centerline at J_f (a) 0.2 and (b) 0.68 m/s for J_g of (○) 0.0, (∗) 0.005, (+) 0.015, (△) 0.1, and (◇) 0.18 m/s.

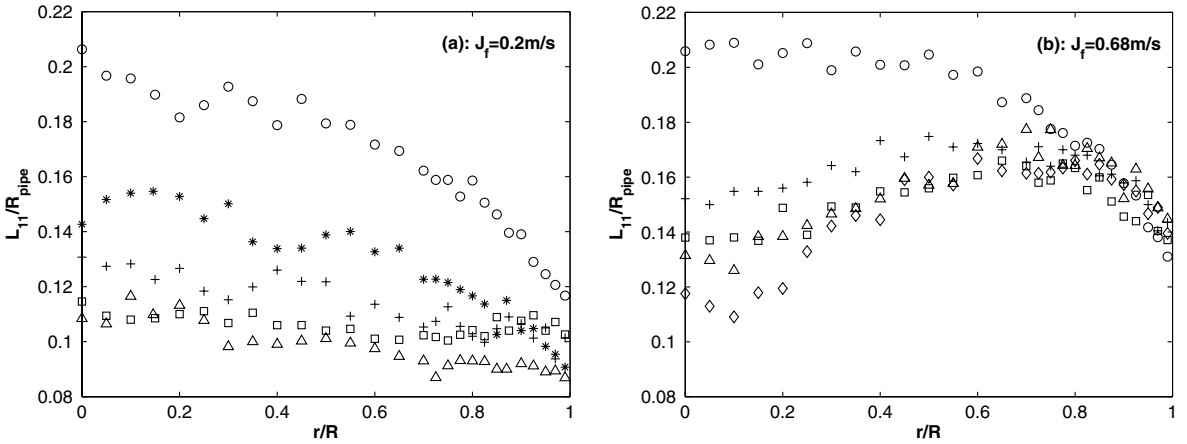

Fig. 9. Radial distribution of the longitudinal integral length scale at J_f (a) 0.2 and (b) 0.68 m/s for J_g of (○) 0.0, (∗) 0.005, (+) 0.015, (□) 0.085, (△) 0.1, and (◊) 0.18 m/s.

wall as shown in Fig. 9(b). The difference in the trends may be related to the radial distribution of the relative velocity, as shown in Fig. 6, where the length scales in the wakes of the bubbles are related to U_r, since the bubble diameter profiles are almost uniform in the pipe core region. However, further investigation of this is required to make more definitive conclusions.

In single phase pipe flows, the area averaged integral length scale scales with the pipe diameter, and is nearly independent of the Reynolds number. For the two-phase bubbly flow, however, the pipe diameter does not represent the characteristic length scale of the continuous phase. The integral length scale in this case will not scale with the pipe diameter. A better representation of the characteristic length scale of the continuous liquid phase in two-phase bubbly flows would be the distance between the bubbles (r_{ch}). Estimates for r_{ch} for the current flow conditions were obtained by assuming an uniform bubble distribution in both the radial and azimuthal directions using the measured void fraction and bubble diameter. The variation of r_{ch} normalized by the bubble diameter with the void fraction is shown in Fig. 10, where additional data sets at different J_f were used to show the correlation for a wider range of experimental conditions. The integral length scale normalized by r_{ch} was not constant in this instance, but increased both with the Reynolds number based on J_f and r_{ch}, and the area averaged void fraction. An empirical correlation for the normalized integral length scale was developed as a function of this Reynolds number and the area averaged void fraction. The correlation given by

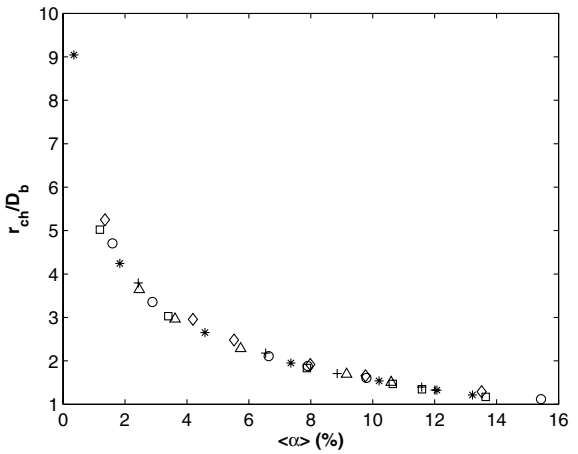

Fig. 10. Variation of the r_{ch} normalized by the bubble diameter with the area averaged void fraction at J_f ((□) 0.2, (∗) 0.26, (+) 0.35, (△) 0.45, (○) 0.58, and (◊) 0.68 m/s).

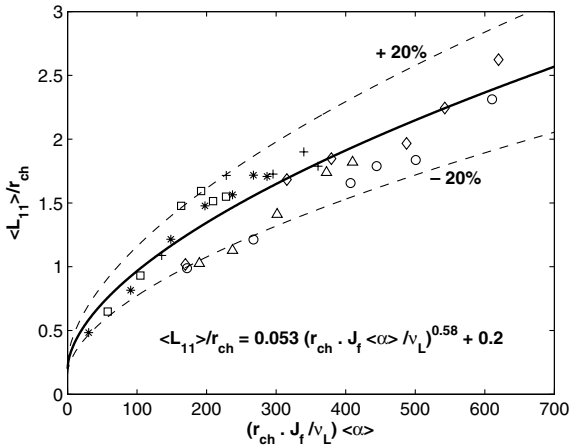

Fig. 11. Effect of Reynolds number based on the liquid superficial velocity, area averaged void fraction, and the characteristic length scale (r_{ch}) on the area averaged integral length scale for present data at J_f ((□) 0.2, (∗) 0.26, (+) 0.35, (△) 0.45, (○) 0.58, and (○) 0.68 m/s).

$$\langle L_{11}\rangle/r_{ch} = 0.053\left(\frac{r_{ch}\cdot J_f\langle\alpha\rangle}{\nu_L}\right)^{0.58} + 0.2 \tag{4}$$

predicts the data to within ±20%, as shown in Fig. 11. For single-phase flow, r_{ch} tends to the pipe radius and the value of $\langle L_{11}\rangle$ in this case will be consistent with previous observations.

4.3. Turbulence energy spectra

The normalized one-dimensional axial ($E_{11}(k_1)$) and radial ($E_{22}(k_1)$) turbulent energy spectra are presented in Figs. 12 and 13 for J_f of 0.2 and 0.68 m/s, respectively. The spectra are plotted in both log–log scale (Figs. 12(a), (b) and 13(a), (b)) and on semi-log scale (Figs. 12(c), (d) and 13(c), (d)). In the semi-log scale, the spectra are multiplied by the wave number so that the area under the curve represents the energy, i.e.,

$$\int_0^\infty \frac{E_{11}(k_1)}{u'^2}k_1\,\mathrm{d}\ln k_1 = \int_0^\infty \frac{E_{22}(k_1)}{v'^2}k_1\,\mathrm{d}\ln k_1 = 1 \tag{5}$$

In these plots, the wave number is presented normalized by the local integral length scale L_{11}. The axial spectra was used to estimate the longitudinal dissipation length scale (λ) as

$$\frac{1}{\lambda^2} = \frac{1}{2\overline{u'^2}}\int_0^\infty k_1^2 E_{11}(k_1)\,\mathrm{d}k_1 \tag{6}$$

The Reynolds number Re_λ based on u' and λ as well as the turbulence length scales at the centerline for the current flow conditions are tabulated in Table 1. The Kolmogorov length scale (η) here was estimated using the values of u' and λ, assuming isotropy. Similar to L_{11}, an increase in the void fraction causes both the dissipation and Kolmogorov length scales to decrease for constant J_f.

In the log–log scale, the single-phase spectra shows the classical (−5/3) slope in the inertial region. The inertial region here was specified to be between k_1L_{11} of 1.3, as suggested by Pope (2001), to the wave number corresponding to the dissipation length scale ($k_\lambda L_{11}$), as shown by the solid vertical lines in the figures. For the radial spectra the dissipation length scale was taken as $\lambda/\sqrt{2}$, assuming isotropy at the pipe centerline for the single-phase case. In the semi-log scale, the single-phase spectra do not show the significant increase in the energy at the beginning of the inertial region as expected due to aliasing, which is most significant at the low wave numbers (Tennekes and Lumley, 1972; Pope, 2001).

In the two-phase flow, increasing the void fraction increases the average liquid velocity for the same J_f, which increases the local *Re* causing a greater separation in the length scales. This is reflected in the spectra, which shows a wider wave number range for the two-phase flow. On the log–log scale, the amplitude of the

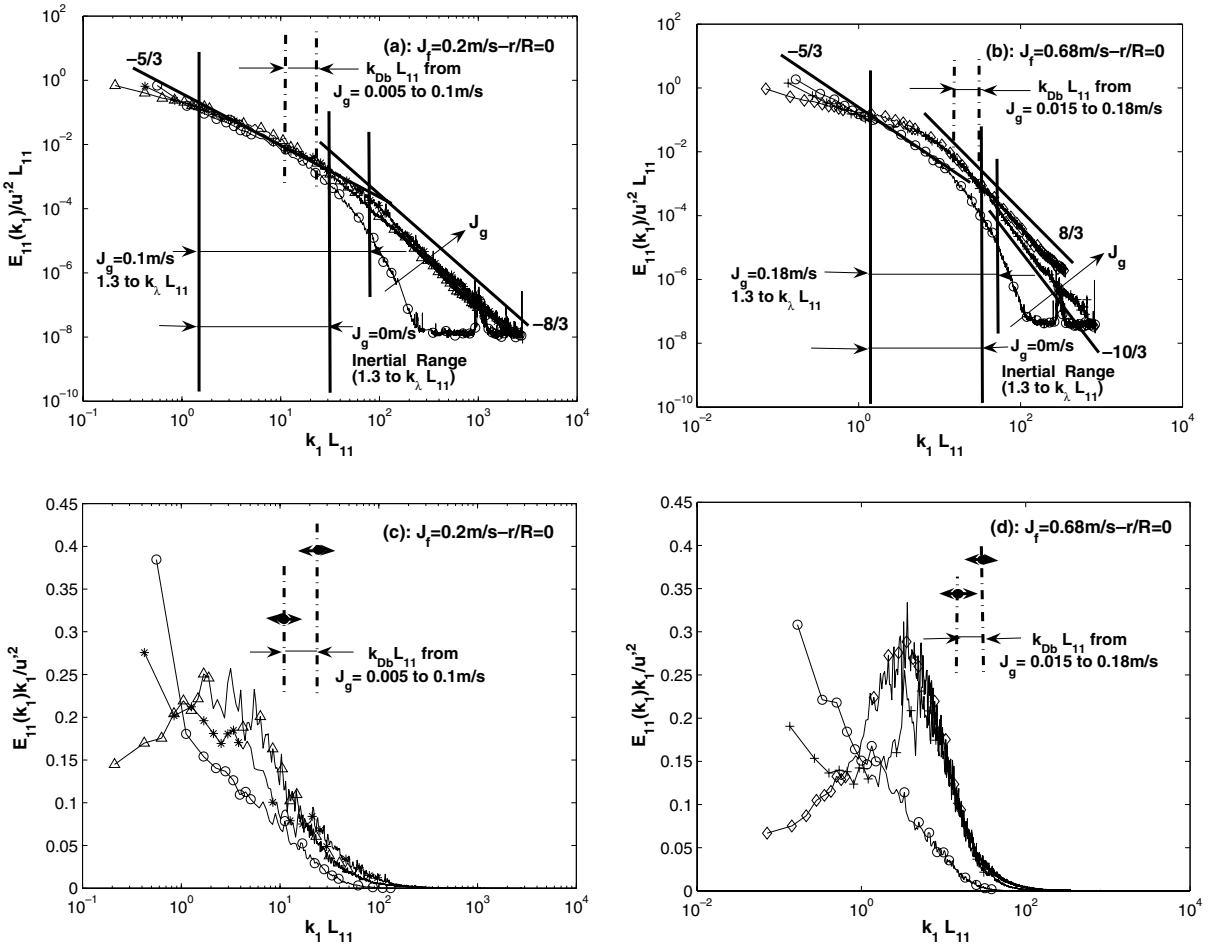

Fig. 12. Axial turbulent energy spectra at the centerline for J_f (a, c) 0.2 m/s for J_g ((○) 0.0, (∗) 0.005, and (△) 0.1 m/s) and (b, d) 0.68 m/s for J_g ((○) 0.0, (+) 0.015, and (◊) 0.18 m/s).

normalized liquid spectra in the two-phase flow is smaller than the single-phase flow at small wave numbers, and increases at the higher wave number indicating a higher turbulence energy content in this range. At the lower J_f of 0.2 m/s (Figs. 12(a) and 13(a)), increasing J_g from 0.005 to 0.1 m/s (corresponding to an increase in $\langle\alpha\rangle$ from 1.2% to 13.6%) has no discernible effect on the slope of the spectra in the region $k_1L_{11} = 1$ up to the wave number corresponding to the dissipation length scale, and is approximately equal to the single phase case. Beyond the dissipation length scale, the spectra falls off much slower than the single phase case, with a constant slope of about (−8/3). For the higher J_f of 0.68 m/s, there is a more pronounced effect on the spectra for approximately the same increase in $\langle\alpha\rangle$ (Figs. 12(b) and 13(b)). The slope of the liquid turbulence spectra does not exhibit a constant value in the range $k_1L_{11} = 1$ up to the wave number corresponding to the dissipation length. Instead, there is a significant increase in the energy over the single phase flow in this wave number range. Beyond the dissipation scale, the spectra again falls off much slower than the single phase flow, with a slope of about (−10/3) at the lower J_g, which increases to (−8/3) at the higher J_g. For the flow conditions shown in Figs. 12 and 13, the bubblance changes from about 3 to 110.

In the two-phase bubbly flow the interaction of the bubbles with the liquid turbulence is expected to lead to additional production and dissipation of turbulence energy. This interaction should be most pronounced at turbulence length scales that are on the same order of the bubble diameter. The wave number range corresponding to the nominal bubble diameters for the different J_g is shown in the Figures by vertical dashed lines. The bubble diameter distributions from the nominal diameter for the two end cases are represented by two

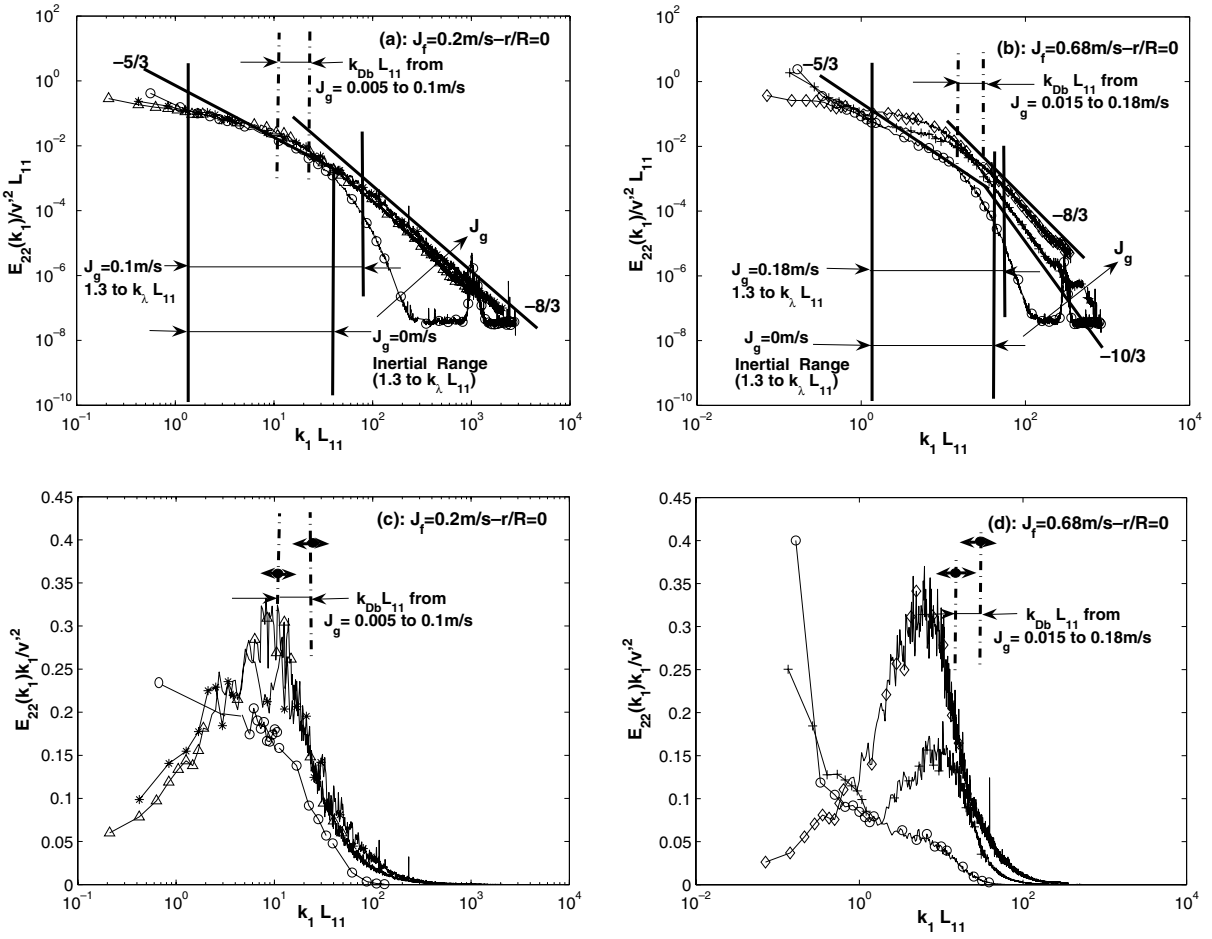

Fig. 13. Radial turbulent energy spectra at the centerline for J_f (a, c) 0.2 m/s for J_g ((○) 0.0, (∗) 0.005, and (△) 0.1 m/s) and (b, d) 0.68 m/s for J_g ((○) 0.0, (+) 0.015, and (◇) 0.18 m/s).

Table 1
Experimental conditions and corresponding turbulence length scales at $r/R = 0.0$

J_f (m/s)	J_g (m/s)	$\langle\alpha\rangle$(%)	L_{11} (mm)	λ (mm)	η (mm)	Re_λ
0.2	0.0	0.0	20.6	4.6	0.29	45
0.2	0.005	1.2	14.3	0.9	0.05	58
0.2	0.015	3.4	13.1	0.8	0.04	59
0.2	0.085	11.6	11.5	0.8	0.03	115
0.2	0.1	13.6	10.8	0.7	0.03	121
0.68	0.0	0.0	20.6	4.1	0.15	143
0.68	0.015	1.4	15.2	2.2	0.07	161
0.68	0.085	8.0	13.8	1.8	0.05	282
0.68	0.1	9.8	13.1	1.6	0.04	297
0.68	0.18	13.5	11.7	1.4	0.03	315

arrows emanating from the wave number corresponding to the nominal bubble diameter (k_{D_b}). It is clear that the bubble diameter range lies within the integral and dissipation length scales as shown in Figs. 12 and 13. Hence, in the two-phase bubbly flow, there could be significant energy production within the traditionally defined inertial region. This can be illustrated more clearly in the semi-log scale, as shown in Figs. 12(c), (d) and 13(c), (d). For the single phase flow, the curve does not show the expected increase and peak at the

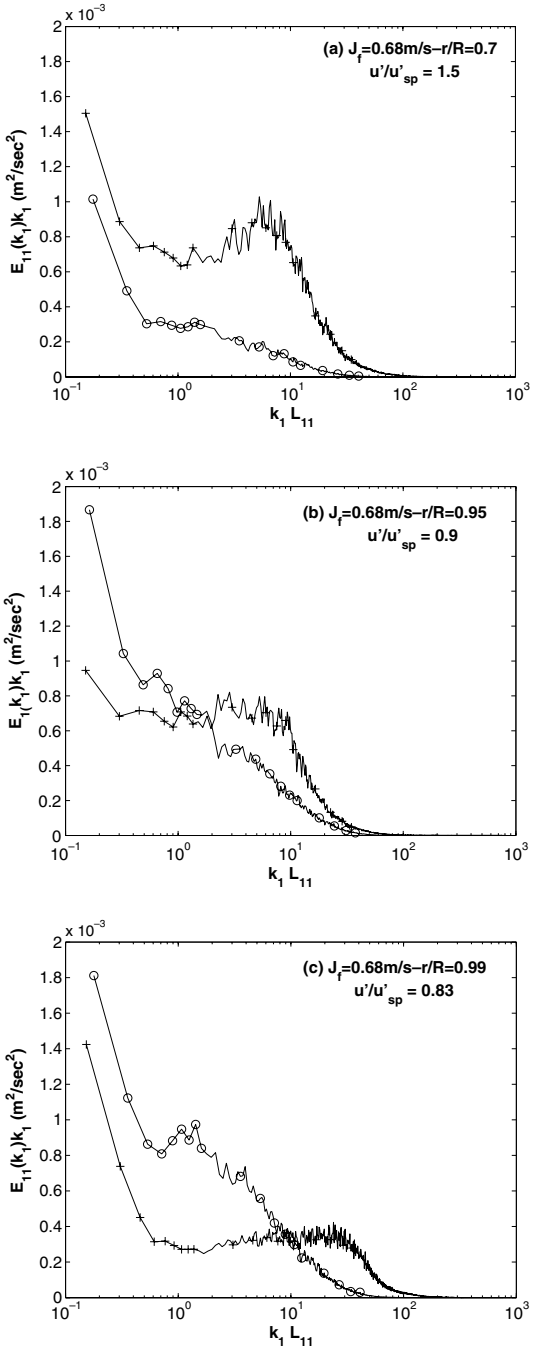

Fig. 14. Axial turbulent energy power spectra as the wall is approached in a suppression case for $J_f = 0.68$ m/s and J_g ((○) 0.0 and (+) 0.015 m/s).

end of the production region. This is due to the aliasing at the lower wave numbers as mentioned earlier. Typically, the curve would then decrease through the inertial region and approach zero at the dissipation length scales. This region is clearly seen in the figures for the single phase flow. For the bubbly flow, however, there is a significant energy addition within the scales from the integral to the dissipation length scale. For example, at $J_f = 0.2$ m/s and $J_g = 0.005$ m/s, the spectral curve initially decreases as in the single-phase flow, but then

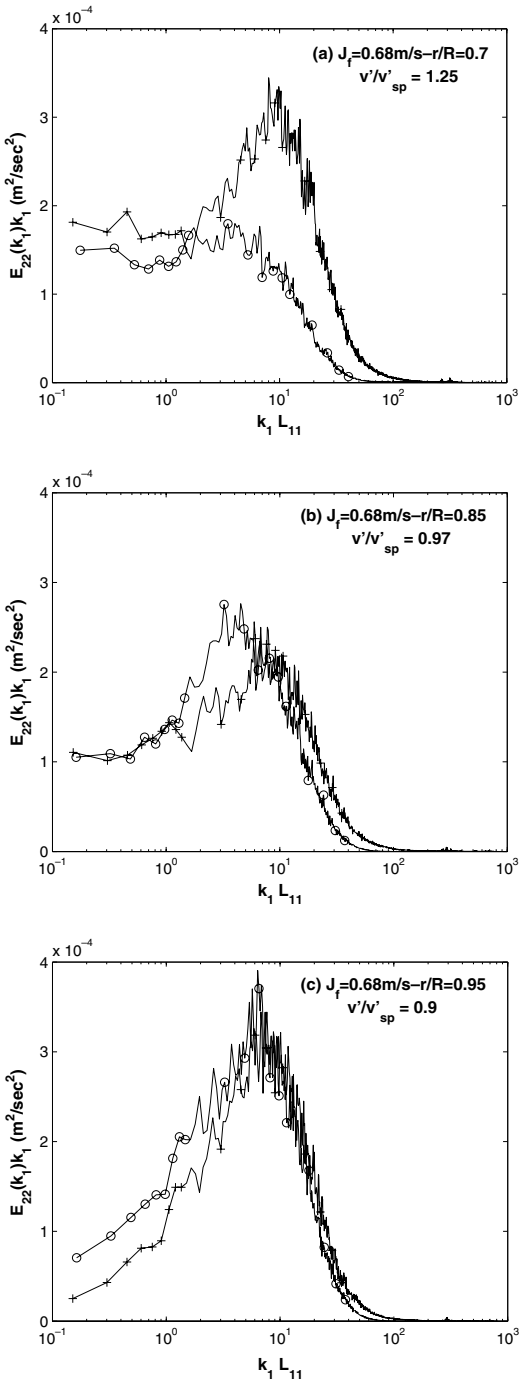

Fig. 15. Radial turbulent energy power spectra as the wall is approached in a suppression case for $J_f = 0.68$ m/s and J_g ((○) 0.0 and (+) 0.015 m/s).

increases above the single phase curve around k_1L_{11} of 3, signifying a production of energy in this wave number range (Fig. 12(c)). This is more clearly evident at the higher J_f of 0.68 m/s and J_g of 0.015 m/s (Fig. 12(d)). The amount of energy contained within this wave number range increases as J_g is increased. At the highest J_g for both J_f, the spectral curve on the semi-log scale does not exhibit the initial decrease. Instead, there is a

continuous increase and the curve reaches a maximum in the range of wave numbers between the integral and dissipation scales, indicating that the most significant energy containing eddies in this case are in this wave number range. The spectral curves may be explained by relating the increase in the energy at the higher wave number range to the energy production due to the relative motion between the phases. This additional energy is expected to be a maximum in the range of length scales that are comparable to the bubble diameter. At low J_g, there is only a small decrease in the integral length scale, and hence the change in the spectra at the low wave number range would be small. However, the additional energy production due to the bubbles would increase the energy in the wave number range comparable to the bubble diameter range. As J_g increases, there is a more significant decrease in the integral length scale, which shifts the turbulence production to higher wave numbers in absolute terms. The bubble diameter D_b increases with an increase in J_g, and the energy addition due to the bubbles will move to smaller wave numbers. At a sufficiently high J_g, it is plausible that there would be an overlap so that the curve will show a continuous increase with one maximum, as seen at the highest J_g in Fig. 12(c) and (d). The radial spectra show similar characteristics as shown in Fig. 13(c) and (d). However, the maximum bubble–turbulence interaction occurs at a lower wave number range. Generally, as J_g is increased the energy containing eddies are shifted to smaller wave numbers and are within the wave number range corresponding to the bubble diameter distribution. In the current experiments, the range of length scales where the maximum interaction occurs was within 2.5–6.5 times the bubble diameter, which is approximately in the same range of the variation of the r_{ch} for J_f of 0.2 and 0.68 m/s (Fig. 10). This indicates that the maximum interaction occurs at length scales comparable to r_{ch}.

A turbulence suppression was observed at $J_f = 0.68$ and $J_g = 0.015$ m/s as the wall was approached, starting from $r/R \gtrsim 0.9$ for u'/U and $r/R \gtrsim 0.8$ for v'/U, as shown in Fig. 7(b) and (d). The axial and radial turbulence energy spectra for these conditions are shown on a log-liner scale in Figs. 14 and 15. The corresponding single phase data at the same J_f are shown for comparison. The spectra at three different radial locations are presented, corresponding to a case where there is turbulence augmentation and then increasing turbulence suppression. The three conditions are quantified by the ratio of the turbulent velocity relative to the corresponding single phase value at the same J_f, and are given in the figures. The spectra in this case are not normalized so that the area under the curves represents the turbulence energy due to each velocity component ($\overline{u'^2}$ and $\overline{v'^2}$). Under the turbulence augmentation condition at $r/R = 0.7$ (Figs. 12(a) and 13(a)), there is an increase in the energy over the entire range of scales. As the first suppression condition is reached (Figs. 12(b) and 13(b)), the liquid turbulence energy initially decreases below the single phase flow case only at the low wave number range, while it remains higher at the higher wave number range. This is somewhat surprising, as this indicates that the turbulence energy is initially lost at the large length scales, while dissipation is predominantly a small scale phenomena. As the suppression increases, the wave number range over which the suppression occurs extends to higher wave numbers as seen in Figs. 12(c) and 13(c). This suggests that the turbulence energy is initially lost directly to the bubbles through an inviscid transfer of energy at the larger scales, and then progressively moves to the smaller scales. The suppression does not occur over the same wave number range in radial and axial direction where its range in the radial spectra is wider.

5. Conclusions

Experiments were performed in a 200 mm diameter vertical pipe to investigate the liquid turbulence structure of co-current two-phase air–water bubbly flow. The water superficial velocity was 0.2 and 0.68 m/s, and the gas superficial velocity was in the range 0–0.18 m/s, corresponding to an area average void fraction variation from 1.2% to 13.6%. The bubble characteristics were measured using a dual optical probe while the liquid turbulence characteristics were measured using hot film anemometry.

A core-peak void fraction distribution was obtained for most flow condition, except at very low void fraction flows where a wall-peak was observed. The wall-peak profile was associated with an increase in the bubble diameter towards the pipe wall. The average liquid velocity profile was more uniform than the single phase profile when there was a wall-peak void fraction profile, while it showed higher average velocities in the core region for the core peak void fraction profiles. In general, there is an increase in the turbulence intensity when the bubbles are introduced into the flow. However, a turbulence suppression was observed close to the wall at a very low void fraction flow. The turbulence integral length scale decreased with an increase in the gas flow

rate or void fraction due to the break-up of the continuous liquid phase. The area averaged integral length scale, normalized by a characteristic length scale (r_{ch}) that represents the distance between the bubbles, was found to correlate with the Reynolds number based on J_f and r_{ch}, and the area averaged void fraction.

There is a significant turbulence energy production in the range of wave numbers between the integral and dissipation scales. The range of nominal bubble diameter lies within this wave number range, suggesting that this energy production is likely due to the bubble liquid interaction. Hence, the traditional concept of an inertial range where there is no significant production or dissipation may not be valid in two-phase bubbly flows. A suppression of the turbulence was observed at very low void fraction flows close to the wall. Under the turbulence suppression conditions, the spectra showed that the suppression initially occurs over the small wave number range or at the large length scales. As the suppression increased, this range extended to higher wave numbers.

References

Browne, L., Dinkelacker, A., 1995. Turbulent pipe flow: pressure and velocities. Fluid Dyn. Res. 15, 177–204.

Browne, L., Antonia, R.A., Chua, L., 1989. Calibration of *x*-probes for turbulent flow measurements. Exp. Fluids 3, 201–208.

Bruun, H.H., 1995. Hot Film Anemometery – Principles and Signal Analysis. Oxford University Press.

Farrar, B., Samways, A., Ali, J., Bruun, H., 1995. A computer-based hot-film technique for two-phase flow measurements. Measur. Sci. Technol. 6, 1528–1537.

Gore, R.A., Crowe, C.T., 1989. Effect of particle size on modulating turbulence intensity. Int. J. Multiphase Flow 15, 279–285.

Hibiki, T., Ishii, M., 1999. Experimental study on interfacial area transport in bubbly two-phase flows. Int. J. Heat Mass Transfer 42, 3019–3035.

Kataoka, I., Serizawa, A., 1989. Basic equations of turbulence in gas–liquid two-phase flow. Int. J. Multiphase Flow 15, 843–855.

Lahey Jr., R.T., Lopez de Bertodano, M., Jones Jr., O.C., 1993. Phase distribution in complex geometry conduits. Nucl. Eng. Des. 141, 177–201.

Lance, M., Bataille, J., 1991. Turbulence in the liquid phase of a uniform bubbly air–water flow. J. Fluid Mech. 222, 95–118.

Laufer, J., 1954. The structure of turbulent in fully developed pipe flow. NACA, 1174.

Lawn, C.J., 1971. The determination of the rate of dissipation in the turbulent pipe flow. J. Fluid Mech. 48, 477–505.

Liu, T.J., 1989. Turbulence modeling in bubbly two-phase flows. Ph.D. thesis, Northwestern University.

Liu, T.J., 2002. An effective signal processing method for resistivity probe measurements in a two-phase bubbly flow. Measur. Sci. Technol. 13, 206–217.

Liu, T.J., Bankoff, S.G., 1993. Structure of air–water bubbly flow in a vertical pipe (i and ii). Int. J. Heat Mass Transfer 36, 1049–1072.

Lopez de Bertodano, M., 1998. Two fluid model for two-phase flow turbulent jets. Nucl. Eng. Des. 179, 65–74.

Michiyoshi, I., Serizawa, A., 1986. Turbulence in two-phase bubble flow. Nucl. Eng. Des. 95, 253–267.

Ohnuki, A., Akimoto, H., 2000. Experimental study on transition of flow pattern and phase distribution in upward air–water two-phase flow along a large vertical pipe. Int. J. Multiphase Flow 26, 367–386.

Ohnuki, A., Akimoto, H., 2001. Model development for bubble turbulent diffusion and bubble diameter in large vertical pipes. J. Nucl. Sci. Technol. 38, 1074–7080.

Pope, S., 2001. Turbulent Flows. Cambridge University Press.

Rensen, J., Luther, S., Lohse, D., 2005. The effect of bubbles on developed turbulence. J. Fluid Mech. 538, 153–187.

Revankar, S., Ishii, M., 1992. Local interfacial area measurement in bubbly flow. Int. J. Heat Mass Transfer 35, 913–925.

Schlichting, H., 1979. Boundary Layer Theory. McGraw Hill, NewYork.

Serizawa, A., Kataoka, I., 1990. Turbulence suppression in bubbly two-phase flow. Nucl. Eng. Des. 122, 1–16.

Shoukri, M., Hassan, Y., Gerges, I., 2003. Two phase bubbly flow structure in large diameter vertical pipe. Can. J. Chem. Eng. 18, 205–211.

Sun, X., Smith, T.R., Kim, S., Ishii, M., Uhle, J., 2003. Interfacial structure of air–water two-phase flow in a relatively large pipe. Exp. Fluids 34, 206–219.

Tennekes, H., Lumley, J., 1972. A First Course in Turbulence. Massachusetts Institute of Technology Press, Massachusetts.

Uga, T., 1972. Determination of bubble-size distribution in bwr. Nucl. Eng. Des. 22, 252–261.

Van Fossen, G., Simoneau, R., Ching, C.Y., 1995. Influence of turbulence parameters, Reynolds number, and body shape on stagnation region heat transfer, Technical Report TP3487, NASA.

Wang, G., Ching, C.Y., 2001. Measurement of multiple gas-bubble velocities in gas–liquid flows using hot-film anemometry. Exp. Fluids 31, 428–439.

Wang, S.K., Lee, S.J., Jones Jr., O.C., Lahey Jr., R.T., 1987. 3-d turbulence structure and phase distribution measurements in bubbly two-phase flows. Int. J. Multiphase Flow 13, 327–343.

Wang, S.K., Lee, S., Jones, O., Lahey, R., 1990. Statistical analysis of turbulent two-phase pipe flow. J. Fluids Eng. 112, 89–95.

Yoneda, K., Yasuo, A., Okawa, T., 2002. Flow structure and bubble characteristics of steamwater two-phase flow in a large-diameter pipe. Nucl. Eng. Des. 217, 267–281.